Energy Advances

ROYAL SOCIETY OF CHEMISTRY

PAPER

View Article Online
View Journal | View Issue

Cite this: *Energy Adv.*, 2023, 2, 137

Cation synergy in Sr and Al substituted $LaMnO_3$ during solar thermochemical CO_2 splitting†

Mahesh Muraleedharan Nair and Stéphane Abanades *

Received 9th November 2022,
Accepted 1st December 2022

DOI: 10.1039/d2ya00309k

rsc.li/energy-advances

Perovskites (ABO_3) constitute an important category of oxygen carriers for applications in thermochemical redox processes. This study aims to derive the relationship of cation dependent parameters including the tolerance factor (τ), critical radius (R_c), free volume (V_F), electronegativity (χ), and metal–oxygen bond energy (λ) with O_2/CO evolution efficiencies during redox steps of $La_xSr_{1-x}Mn_yAl_{1-y}O_3$ (x = 0.4, 0.5, and 0.6 and y = 0.4, 0.5, 0.6, and 0.75) perovskite series. Such parameters can reflect the lattice structural variations and bond polarity in these materials. The observed trends of O_2/CO evolution are nearly reversed, with regard to the variations in cation constitution. Inconclusive correlations were observed for τ, R_c, and V_F during reduction and re-oxidation, indicating that the role of these parameters in representing the observed redox behaviour is limited. In contrast, the cation electronegativities and metal–oxygen bond energies were found to induce a significant impact in depicting the redox chemistry of these materials. Rather than the individual effects, the entire cationic constituents are found to synergistically influence the reduction and re-oxidation reactions of the oxygen carriers used in this study. Direct relationships are observed for the calculated values of both χ and λ with the experimentally derived O_2/CO evolution. The outcomes of this study can possibly influence the design of oxygen carriers with an improved performance in thermochemical processes for converting CO_2 and utilizing solar energy.

1. Introduction

Environmentally friendly energy technologies are strongly desired either to diminish or to totally eliminate the dependence on fossil derived fuels. Redox processes involving chemical reactions taking place in separate reduction/oxidation steps at high temperatures offer tremendous potential in this regard.[1–3] One such process receiving considerable attention is related to the thermochemical splitting of CO_2/H_2O over metal oxide oxygen carriers, utilizing concentrated solar energy (CSE).[4–6] The measure of deviation from oxygen stoichiometry (non-stoichiometry, δ) of the oxygen carrier plays a crucial role in deciding the overall process efficiency. In terms of superior reaction kinetics and thermochemical stability, non-stoichiometric oxides are mostly preferred as oxygen carriers for thermochemical reactions.[1–6] High operating temperatures were generally required for the benchmark ceria (CeO_2) based oxygen carriers. The addition of doping cations in substitution to cerium promotes the oxygen mobility and creation of oxygen vacancies in the ceria fluorite lattice, which in turn enhances the reduction capability of ceria-based mixed oxides in comparison with pure ceria. As a result, it has been demonstrated that the incorporation of cerium oxide with other metals gives rise to mixed oxides that can be reduced at lower temperatures than pure ceria.[7] In return, the oxidation rates of the mixed ceria compounds are drastically lowered in comparison with those of pure ceria.[8] In other words, the oxidation step is hindered when the reduction step is facilitated, and *vice versa*. This persuaded the quest for alternative materials, among which perovskite structured complex oxides were found to be the most effective.[1,2,9–11] In this case, the ABO_3 structure can accommodate a large number of cationic substitutions in varying proportions in the crystal lattice, thereby allowing long-range tailoring of the redox chemistry of these materials. In solar thermochemical redox processes, the most encouraging performance so far was reported for materials with manganese in the B-site, along with lanthanum and strontium together occupying the A-site (*e.g.*, $La_xSr_{1-x}MnO_3$).[12–16] Several other combinations were explored where issues regarding limited redox efficiency, thermal stability, or kinetic reaction rates were frequently encountered.[14,15] Therefore, studies are still ongoing to identify an optimum perovskite composition for the advancement of this interesting approach for solar energy harvesting. Introducing cationic mismatch in the A/B-site could be one appropriate way

Processes, Materials and Solar Energy Laboratory, PROMES-CNRS (UPR 8521), 7 Rue du Four Solaire, 66120, Font-Romeu, France.
E-mail: Stephane.Abanades@promes.cnrs.fr; Tel: +33(0)4-68-30-77-30

† Electronic supplementary information (ESI) available: Additional figures correlating experimental redox profiles. See DOI: https://doi.org/10.1039/d2ya00309k

to modify the thermochemical redox behaviour of perovskite oxides. Apart from the nature, the amount of cationic substituents was found to be crucial in this regard. Structural variations, electron distributions, cation exsolution or unusual oxidation states thus arise, and can contribute towards higher redox reaction extents, enhanced oxygen mobility and oxygen vacancy concentration, as desired for efficient oxygen carriers. However, further fundamental understanding is necessary to identify appropriate combination of elements that can be used as cations in mixed metal oxides.

Information regarding the influence of cation dependent parameters on the thermochemical redox activity can supplement the compositional optimization of perovskite oxygen carriers. In this regard, one straightforward and facile strategy is to deduce the relationships between simple structural aspects with experimentally obtained data. Previously, Liu *et al.* used transition metal electronegativities to describe the trends in oxygen storage capacity among a series of perovskites.[17] In another study, Wang *et al.* observed that the ignition behaviour of a series of substituted perovskites was related to variations in the calculated values of electronegativity and bond energy.[18] More recently, Nair *et al.* derived the correlation between the amounts of oxygen and CO evolved during the two-step thermochemical redox process, with geometrical parameters such as critical radius and lattice free volume, respectively, in a series of A-site substituted manganite perovskites.[19] Depending on the variations in the A/B-site cationic composition, several such metrics can be recognized that may independently or synergistically control the thermochemical redox behaviour of perovskite oxides. For instance, the value of Goldschmidt tolerance factor (τ) is primarily dependent on the entire cationic composition and is considered as a measure of deviation from the ideal cubic structure. The extent of this structural distortion can be important for facilitating the bulk to surface (or *vice versa*) oxygen mobility, one major requirement for thermochemical redox applications.[20,21] Similarly, variations in cation electronegativity (χ) or metal–oxygen bond energy (λ) can contribute towards describing the thermochemical redox properties of oxygen carriers.

Partial substitution of cationic elements in varying amounts results in lattice structural defects, thus facilitating oxygen vacancy formation and influencing bond polarity. The resultant lowering of activation energies for electron and oxygen ion transport favours rapid release and uptake of oxygen, as required for thermochemical redox reactions. Proposing a relevant indicator by accommodating all the possible perovskite-based oxygen carriers can be promising. However, it is to be noted that several other phenomena such as sintering, phase decomposition, carbonate formation, *etc.*, are to be considered and cannot be ruled out. A limited number of perovskite oxides exhibited the potential to overcome the aforementioned stability concerns. Among these, an even fewer number of materials were studied by systematically varying the A/B site compositions. The incorporation of Sr and Al respectively at the A- and B-sites was previously found to influence the redox properties of $LaMnO_3$.[22–28] LSMA materials ($La_xSr_{1-x}Mn_yAl_{1-y}O_3$) were selected chiefly because they represent one of the most attractive perovskite-based compositions for solar-driven thermochemical CO_2 splitting. Currently, they are among the most performing materials in terms of thermochemical stability, redox activity, CO_2 splitting ability, and fuel production capacity. While the presence of Sr can strongly influence the thermal reducibility, the presence of Al can eliminate the surface carbonate formation that may arise due to Sr segregation.[15,27] Therefore, LSMA is a suitable choice to obtain relevant information regarding the derivation of a general descriptor for thermochemical redox properties. The materials used in this study cover a large span of compositional space in the LSMA perovskite series. Long term performance and compositional stability of these materials during thermochemical redox cycles were previously confirmed.[13,22,25,27] This approach is novel and never used before to provide key indicators about the selection, suitability and relevance of a given material formulation for CO_2 splitting. Therefore, in the present study, a series of $La_xSr_{1-x}Mn_yAl_{1-y}O_3$ perovskites were prepared and their thermochemical oxygen release and subsequent CO_2 splitting efficiencies were experimentally determined. The values thus obtained, along with the corresponding reaction rates, were correlated with the calculated values of tolerance factor, critical radii, lattice free volumes, electronegativities, and metal–oxygen bond energies. These parameters are indicators that reflect the crystal lattice distortion of the perovskite caused by cationic substitution to induce oxygen vacancies. The most obvious connections were observed for the amounts of O_2/CO released with overall cation electronegativities (χ_{AB}) and average metal–oxygen bond energies (λ) among the series of materials considered in this study.

2. Experimental

2.1 Synthesis of materials

The syntheses of multi-cation (Sr and Al) substituted $LaMnO_3$ perovskites were carried out by following the Pechini method. Metal nitrates, citric acid and ethylene glycol were used as precursors. Appropriate amounts of metal nitrates depending on the stoichiometry of the final perovskite were dissolved in an aqueous solution of citric acid. A pre-determined amount of ethylene glycol was then added, and the resultant solution was stirred for 4 h, Afterwards, the solution was dried at 80 °C for 48 h and the dry foamy mass obtained was ground well and calcined under air for 2 h at 1400 °C. The amount of citric acid was chosen so as to attain a molar ratio of 1.5 with total metal ions, and the citric acid:ethylene glycol ratio was fixed at 3 : 2. The calcination temperature was chosen by considering the desired pure phase formation, structure and phase stability under the reaction conditions and melting points of the metallic components used. The materials thus obtained are designated as $La_{0.4}Sr_{0.6}Mn_{0.6}Al_{0.4}O_3$ (LSMA-6,4), $La_{0.6}Sr_{0.4}Mn_{0.6}Al_{0.4}O_3$ (LSMA-4,4), $La_{0.6}Sr_{0.4}Mn_{0.4}Al_{0.6}O_3$ (LSMA-4,6), $La_{0.5}Sr_{0.5}Mn_{0.75}Al_{0.25}O_3$ (LSMA-5,2.5), and $La_{0.5}Sr_{0.5}Mn_{0.5}Al_{0.5}O_3$ (LSMA-5,5).

2.2 Characterization

The formation, purity and crystallinity of the desired perovskite oxygen carriers were assessed by performing X-ray diffraction (XRD) analysis. A Philips PW1820 diffractometer with the Cu Kα radiation (0.15418 nm, angular range 2θ = 20–80°, steps = 0.02 2θ, recording time = 2 s) was used. Standard diffraction patterns (powder diffraction file PDF-2, International Centre for Diffraction Data, ICDD) were used to compare and confirm the formation of the appropriate phase.

2.3 Thermochemical redox experiments

Thermochemical reduction and re-oxidation extents of the perovskite oxides were determined by performing thermogravimetric analyses (TGA) using a SETARAM SETSYS Evolution device (0.03 μg resolution) equipped with a platinum crucible. Mass variations during reduction and re-oxidation steps were continuously monitored as a function of temperature and time. Prior to the redox experiments, blank runs were carried out to eliminate the possible minor baseline drifts due to gas expansion or buoyancy effects. Each analysis was performed using approximately 100 mg of perovskite material in the powder form. A thermal reduction step was performed under an Ar flow of 0.020 NL min^{-1} (99.999% purity, with <2 ppm O_2) at a fixed temperature of 1400 °C during 45 min of temperature plateau. Subsequent re-oxidation step was performed under CO_2 (50% in Ar) at 1050 °C for 60 min. All heating and cooling steps followed a ramp rate of 20 °C min^{-1}. The mass variations were used to determine the number of moles of oxygen (n_{O_2}) released during thermal reduction ($n_{O_2} = \Delta m_{red}/M_{O_2}$) and number of moles of CO (n_{CO}) produced during re-oxidation ($n_{CO} = \Delta m_{oxi}/M_O$).

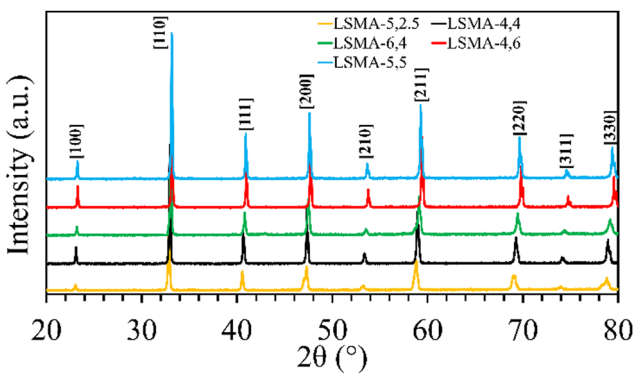

Fig. 1 Wide angle powder XRD patterns observed for a series of $La_xSr_{1-x}Mn_yAl_{1-y}O_3$ oxygen carriers synthesized using the Pechini method, calcined at 1400 °C.

3. Results and discussion

Formation of the appropriate pure phase materials with significant extent of crystallinity is one fundamental requirement for obtaining the desired performance in mixed metal oxides. Therefore, all the synthesized materials used in this study were analysed initially by X-ray diffraction and the obtained diffractograms are shown in Fig. 1. The peaks observed in the wide-angle region for $La_xSr_{1-x}Mn_yAl_{1-y}O_3$ oxygen carriers calcined at 1400 °C were found to belong to the characteristic perovskite structure and slight disparities in peak positions were in accordance with the variations in the cationic constituents. The average crystallite sizes of these materials were determined by using the Scherrer equation. The resultant values varied between 40 and 80 nm and are shown in Table 1. The B-site composition seems to influence the crystallite size since a steady increase was observed with regard to the amount of aluminium incorporated in the material. Information regarding the redox performance of these phase pure perovskites was then gathered by carrying out thermogravimetric analysis. At first, the mass variations during thermochemical reduction (1400 °C) were continuously monitored (ESI,† Fig. S1) and the corresponding amount of oxygen released from these materials were calculated. The obtained O_2 evolution profiles as a function of time are shown in Fig. 2(a). Numerical differentiation of these profiles provided the maximum value for O_2 evolution (thermal reduction) rates, and the profiles are given in the ESI,† Fig. S2. The amounts of O_2 evolved and the reduction rates (Table 1) seem to depend on the amount of Sr in the perovskite oxygen carrier. Apart from the lattice structural modifications, the introduction of Sr in the A-site can result in an increase in the formal oxidation state of Mn (between 3+ and 4+). This change in the oxidation state can be an immediate justification one could find for the experimental O_2 evolution trends. On a detailed observation, LSMA-4,4 and LSMA-4,6 contain the same amount of Sr (40%) in the structure, and the amounts of O_2 evolved are 208 μmol g^{-1} and 273 μmol g^{-1}, respectively.

In this case, the variation in the amount of O_2 evolved at constant Sr concentration may be attributed to the changes in the Al content in the B-site.

Furthermore, the variations in the amounts of O_2 evolved were observed for LSMA-5,2.5 and LSMA-5,5 (395 μmol g^{-1} and 324 μmol g^{-1}, respectively). Here, in contrast to the above observations, the composition of the B-site (Al and Mn) also

Table 1 Overview of $La_xSr_{1-x}Mn_yAl_{1-y}O_3$ oxygen carriers used, along with their redox performance during thermochemical reduction and CO_2 splitting

Material	Crystallite size (nm)	O_2 evolved (μmol g^{-1})	Maximum rate of reduction (μmol g^{-1} s^{-1})	CO evolved (μmol g^{-1})	Maximum rate of re-oxidation (μmol g^{-1} s^{-1})
$La_{0.5}Sr_{0.5}Mn_{0.75}Al_{0.25}O_3$ (LSMA-5,2.5)	40.25	352	0.326	165	0.090
$La_{0.6}Sr_{0.4}Mn_{0.6}Al_{0.4}O_3$ (LSMA-4,4)	53.77	210	0.230	205	0.132
$La_{0.4}Sr_{0.6}Mn_{0.6}Al_{0.4}O_3$ (LSMA-6,4)	51.54	400	0.322	173	0.11
$La_{0.5}Sr_{0.5}Mn_{0.5}Al_{0.5}O_3$ (LSMA-5,5)	63.68	315	0.269	192	0.16
$La_{0.6}Sr_{0.4}Mn_{0.4}Al_{0.6}O_3$ (LSMA-4,6)	77.60	267	0.226	204	0.153

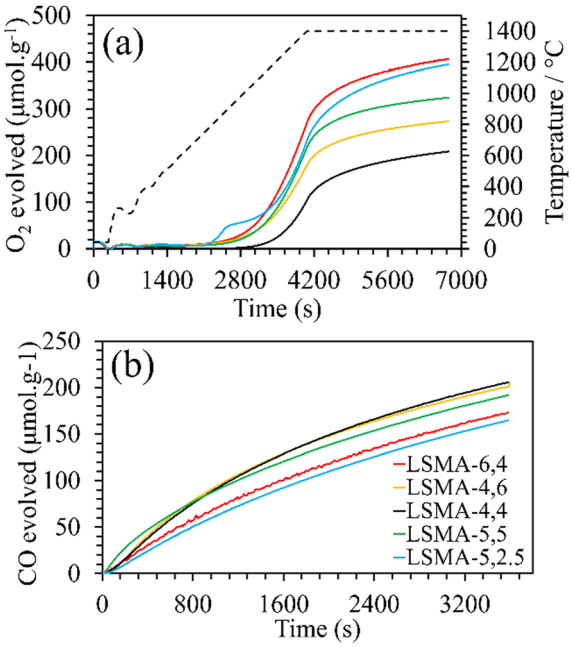

Fig. 2 (a) O_2 evolution profiles derived from mass variation during thermochemical reduction for $La_xSr_{1-x}Mn_yAl_{1-y}O_3$ oxygen carriers. Dashed line represents the temperature variation during reduction (20 °C min^{-1} up to 1400 °C). (b) CO evolution profiles derived from mass variation during CO_2-induced re-oxidation at 1050 °C.

cannot provide a satisfactory explanation for the observed trends. From these results, it can be concluded that rather than variation in the amount of one or more cationic constituents in the composition, the material as a whole synergistically contributes towards the release of oxygen from the perovskite lattice. After achieving a significant extent of reduction, each of these materials was subjected to re-oxidation (isothermal) in the presence of CO_2 (ESI,† Fig. S1). Here again, the mass variations during re-oxidation (1050 °C) were used to obtain the amounts of CO produced, along with the values of CO evolution (re-oxidation) rates. The obtained CO evolution profiles as a function of time are shown in Fig. 2(b). Even though the amounts of CO produced remain smaller in comparison with the amounts of oxygen evolved during reduction (*i.e.*, $n\mathrm{CO} < 2{\cdot}n\mathrm{O_2}$) (Table 1), the trends observed for re-oxidation reflected the observed pattern for oxygen evolution. Interestingly, the materials exhibiting superior efficiency for O_2 evolution were found to be the least effective for CO_2 splitting (reversed trend) under the conditions used in the present study. In other words, the extent of thermochemical reduction cannot be considered as the sole decisive parameter controlling the CO_2 splitting activity of these oxygen carriers. Apart from the cation composition, no parametric alterations were involved either during the synthesis or during the thermochemical redox experiments for the $La_xSr_{1-x}Mn_yAl_{1-y}O_3$ perovskites. Therefore, the observed discrepancies in gas evolution and the corresponding reaction rates can be attributed to the changes in composition of the oxygen carriers. Distorted structures induced by cation element substitution can promote oxygen vacancy formation in the crystal lattice and lower the activation energy of electron and oxygen ion transfer for the CO_2 reduction reaction.

Surface analysis on a series of $La_xSr_{1-x}Mn_yAl_{1-y}O_3$ by Ezbiri *et al.* previously indicated Mn as the redox active element, similar to aluminium free $La_xSr_{1-x}MnO_3$.[27] Therefore, an approximate evolution of the Mn oxidation state in these materials can be derived from the mass variations obtained during thermochemical redox experiments. Assuming complete oxidation during calcination, the formal oxidation state of manganese can be calculated and was found to be close to +4 for all the materials. Thus, during thermochemical reduction, the highest oxidation state fraction of manganese transforms firstly into Mn^{3+}, and subsequently to Mn^{2+}. Since both A and B-site compositions were varied simultaneously, the Mn state in fully oxidized (fresh) materials was not significantly different. In other words, when varying the amount of a single cation, the corresponding changes in the oxidation state are more evident. However, when the amounts of two cations (here Sr and Al) are simultaneously varied, the overall effect is compensated partially. The changes in the manganese oxidation state during O_2 and CO evolution as a function of time are given in Fig. 3. For $La_x^{3+}Sr_{1-x}^{2+}Mn_y^{n+}Al_{1-y}^{3+}O_3^{2-}$, the oxidation state of the redox active Mn element is calculated using the following equation (assuming that Mn is the only reducible cation in the B site that participates in the redox reactions).

$$y \times n = [3 \times 2] - [(x \times 3) + ((1 - x) \times 2) + ((1 - y) \times 3)] \quad (1)$$

Both the amounts of Sr and Al were found to influence the Mn oxidation state of the fresh perovskite oxides. Up to 40% Al

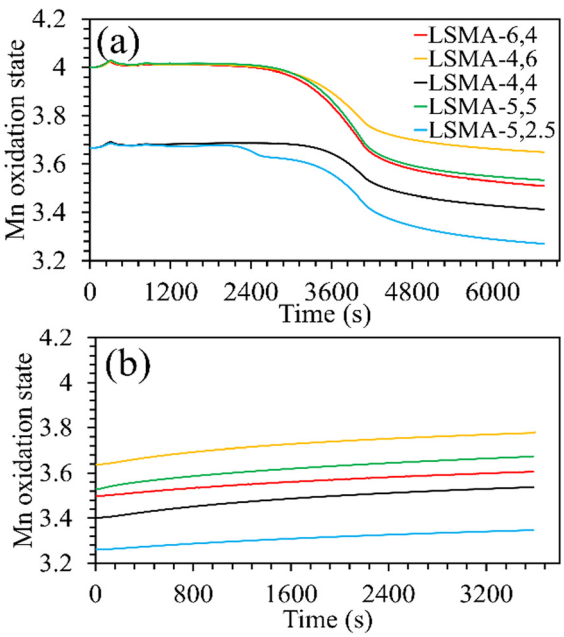

Fig. 3 Evolution of the manganese oxidation state during the (a) thermochemical reduction under Ar and (b) re-oxidation under CO_2, for $La_xSr_{1-x}Mn_yAl_{1-y}O_3$ oxygen carriers.

and 50% Sr in the structure, the oxidation state of manganese remained +3.67, whereas it was +4 for the remaining materials. The final Mn oxidation state after thermochemical reduction varied depending on the overall composition of the perovskites. For example, LSMA-4,6 and LSMA-4,4 had different initial oxidation states for manganese (+4 and +3.67, respectively) and different extents of variation in oxidation states (0.35 and 0.25, respectively). Interestingly, re-oxidation with CO_2 did not bring back the Mn oxidation states to the initial values. Clear distinctions were observed in the final Mn oxidation states, depending on the value at the beginning of CO_2 splitting. However, the extent of variation remained constant (0.14), except for LSMA-6,4 and LSMA-5,2.5 (0.11 and 0.09, respectively). This could be the reason for the observed smaller difference in amounts of CO produced in comparison with the amounts of oxygen evolved during reduction.

Several parameters can be affected by the changes in the size and amount of cations in perovskites. Even though it is widely accepted that an ideal perovskite structure is cubic, cation mismatch can induce deviations.[19,29] In reality, a majority of perovskite oxides exist with structural distortions in the crystal lattice (orthorhombic, rhombohedral, *etc.*) to some extent. One simple parameter considered as a measure of such deviations called tolerance factor (τ) was earlier proposed by Goldschmit.[20,30] It is estimated based on the size and amount of the cationic components along with oxygen, constituting the entire perovskite composition, as shown in eqn (2).

$$\tau = [R_A \cdot x + R_{A'} \cdot (1 - x) + R_O] / \sqrt{2} \cdot [R_B \cdot y + R_{B''} \cdot (1 - y) + R_O] \quad (2)$$

Here, R_N represents the ionic radii of atoms constituting the $A_xA_{1-x}'B_yB_{1-y}'O_3$ structure. A cubic perovskite structure is usually identified by a value of unity for the tolerance factor. However, stable orthorhombic or rhombohedral variants can exist with lower values of τ (between 0.75 and 1) and, for values slightly higher than unity, hexagonal distortions are commonly observed. Structural anomalies thus arise and can have some impact on the crystal symmetry, oxygen mobility and may thereby influence the O_2 release/uptake in these materials. In the present study, τ values were calculated using the ionic radii data tabulated by Shannon[31] and the values varied between 0.98 and 1.005. A graphical representation of O_2 evolution as a function of tolerance factor (Fig. S3, ESI†) resulted in a random distribution without displaying any specific tendencies, indicating that this parameter seldom defined the thermochemical reduction of $La_xSr_{1-x}Mn_yAl_{1-y}O_3$ series. Moreover, a similar distribution was obtained for reduction rates. On the other hand, the amounts of CO evolved, and the corresponding re-oxidation rates exhibited comparatively better correlation, displaying a slightly increasing trend when plotted as a function of the tolerance factor, as shown in Fig. 4. Here, one might probably conclude that a lesser deviation from the ideal cubic structure is favouring thermochemical re-oxidation in the presence of CO_2 in these materials. It is to be noted that the observed tendencies of CO evolution were nearly opposite to the ones observed during thermochemical O_2 evolution (Fig. 2), indicating that the mechanism involved can be similar. However, since such a resemblance is not observed for reduction and re-oxidation while using tolerance factor as a descriptor, the trends observed during re-oxidation cannot be considered conclusive.

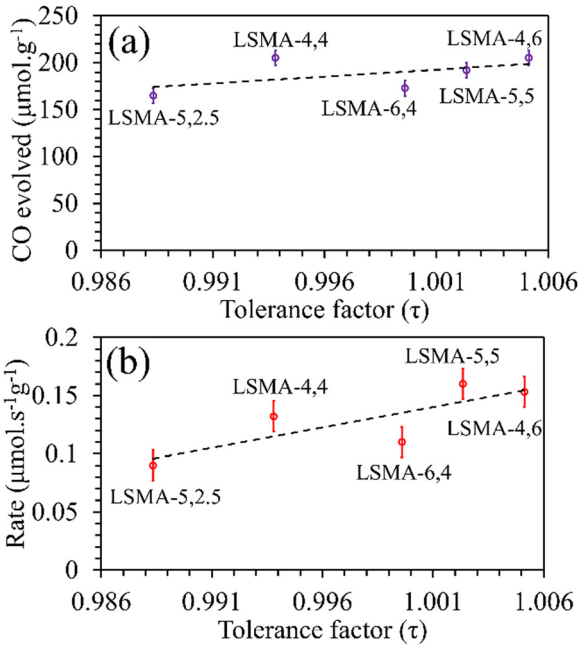

Fig. 4 Amounts of CO evolved (a) and re-oxidation rates (b) as a function of tolerance factor for $La_xSr_{1-x}Mn_yAl_{1-y}O_3$ oxygen carriers.

One frequently used metric to define the anion (O^{2-}) migration in perovskites is the critical radius (R_c), which is defined as the radius of a 3D spherical region, involving two A-site cations and one B-site cation.[32–35] R_c depends on the radii of cations constituting the structure and can be calculated using the following eqns.

$$R_c = [3/4a_0^2 - R_A^2 + R_B^2 - \sqrt{2}a_0R_B] / [2(R_A - R_B) + \sqrt{2}a_0] \quad (3)$$

$$a_0 = 2.15R_B + 2.47 - 1.40\,(\tau^{-1} - 1) \quad (4)$$

Here, a_0 is the pseudo cubic lattice parameter. In general, an increase in R_c values indicates an increase in the volume of 3D space designated for the mobility of oxygen in the lattice, assuming that the effects of all other parameters influencing bulk-surface oxygen transport are negligible. The R_c values obtained for the oxygen carriers used in this study varied between 1.44 and 1.47 Å. As shown in Fig. 5, the plot of the amount of O_2 evolved as a function of the calculated values of critical radius was found to be in agreement with the generally expected trends. Better correlations were observed for the values of O_2 evolution rates, indicating the effectiveness of R_c to describe the O_2 evolution in $La_xSr_{1-x}Mn_yAl_{1-y}O_3$ oxygen carriers. Therefore, further attempts were made to comprehend the role of R_c in CO_2 splitting by these materials and the obtained profiles are shown in Fig. S4 (ESI†). In this case, despite the observed superior correlations, both the amounts of

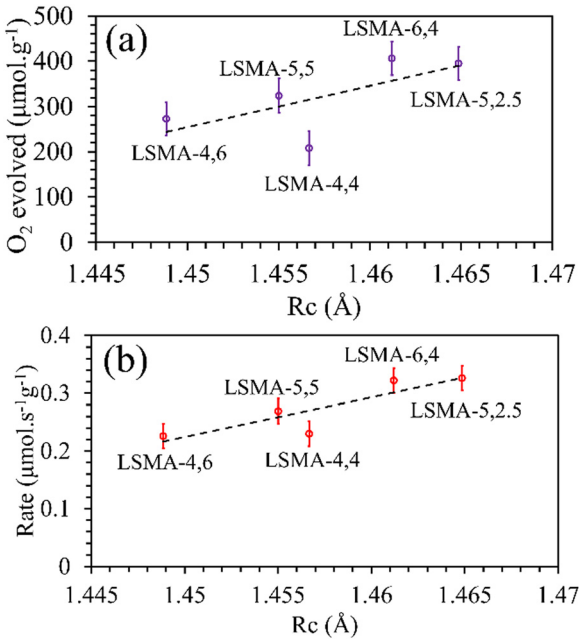

Fig. 5 Amounts of O_2 evolved (a) and reduction rates (b) as a function of critical radius for a series of $La_xSr_{1-x}Mn_yAl_{1-y}O_3$ oxygen carriers.

CO evolved and the corresponding re-oxidation rates were found to sharply decrease with an increase in R_c, indicating that lower values of R_c would favour superior oxygen transport, which is unreasonable. Afterwards, the critical radius per unit cell volume ($R_c{\cdot}u$) was also used to correlate the O_2/CO evolution (Fig. 6 and Fig. S5, ESI†). In this case, the trends and correlations were found to be consistent for CO evolution,

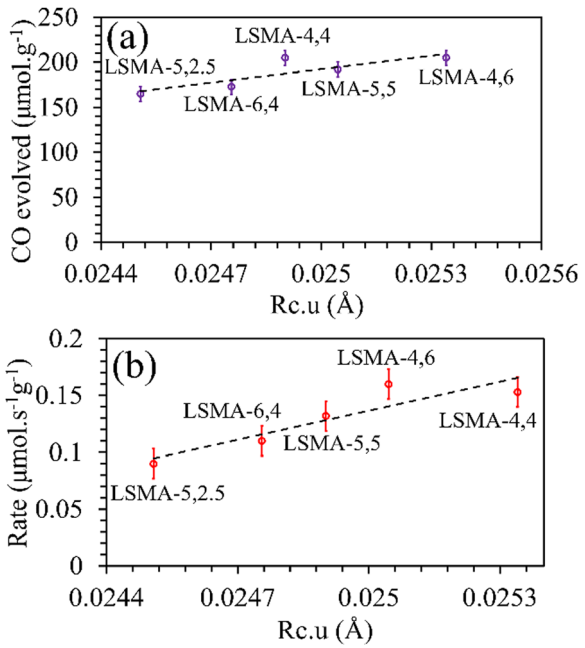

Fig. 6 Amounts of CO evolved (a) and re-oxidation rates (b) as a function of critical radius per unit cell volume for $La_xSr_{1-x}Mn_yAl_{1-y}O_3$ oxygen carriers.

whereas the amount of O_2 evolved was found to decrease with an increase in $R_c{\cdot}u$ and hence, such a trend was irrational. In short, these results cannot satisfactorily explain the observed reversed O_2/CO evolution profiles (Fig. 2). Therefore, the critical radius cannot be considered as a reliable parameter for portraying the thermochemical redox properties of the perovskite series used in this study. Another geometric parameter that could represent the oxygen transport properties in perovskite oxides is the lattice free volume (V_F).[32–34,36,37] This is defined as the difference between the total unit cell volume and the volume occupied by the elemental components in the structure. The activation energy for bulk to surface (or *vice versa*) oxygen transport can be lowered by an increased availability of the free space in the lattice. The calculated values of free volumes and specific free volumes (free volume per unit cell volume, V_F.S) were used to correlate the observed trends in O_2/CO evolution and the corresponding reaction rates (Fig. S6–S9, ESI†). Overall, an increase in geometric parameters (R_c and V_F) indicates an increase in the available path for ion migration, thereby favouring oxygen release/uptake. However, the observed trends reported in Fig. S4, S5 and S7 (ESI†) indicate otherwise. Similarly, regarding specific free volume (ESI,† Fig. S8 and S9), the values of gas evolved (O_2 and CO respectively) varied for same values of V_F.S. Because of such unrealistic trends, geometric parameters can be considered inappropriate to describe the thermochemical redox behaviour of the perovskite oxygen carriers used in this study.

In reality, apart from the aforementioned geometric considerations, the perovskite structure and stability rely on other cation dependent parameters such as electronegativity and metal–oxygen bond strength.[17,18] Electronegativity (χ) is the measure of the tendency of an atom to attract nearby electrons towards itself. The lower the value of electronegativity of the element, the higher will be the ability of the attached oxygen atom to draw the bonding electrons, thereby influencing the thermochemical redox properties of perovskite oxides. In this study, based on previous reports,[17] we initially tried to correlate the values of B-site electronegativities (χ_B), with the amounts of O_2 released and the corresponding reaction rates. The molar average of electronegativities of the B-site cationic constituents on the Pauling scale was used.[38] For $La_xSr_{1-x}Mn_yAl_{1-y}O_3$, the values of electronegativities were calculated using eqn (5)–(7).

$$\chi_A = x \times \chi_{La} + (1 - x) \times \chi_{Sr} \quad (5)$$

$$\chi_B = y \times \chi_{Mn} + (1 - y) \times \chi_{Al} \quad (6)$$

$$\chi_{AB} = \chi_A + \chi_B \quad (7)$$

As shown in Fig. S10 (ESI†), the correlations obtained were not appropriate to portray the O_2 evolution behaviour. For instance, different values of O_2 evolution were obtained for the same value of electronegativity in the case of LSMA-4,4 and LSMA-6,4. Similarly, A-site electronegativities (χ_A) were also found not suitable to depict the amounts of O_2 evolved and reduction rates (Fig. S11, ESI†). Therefore, we calculated the overall cation electronegativity (χ_{AB}) of the entire cationic

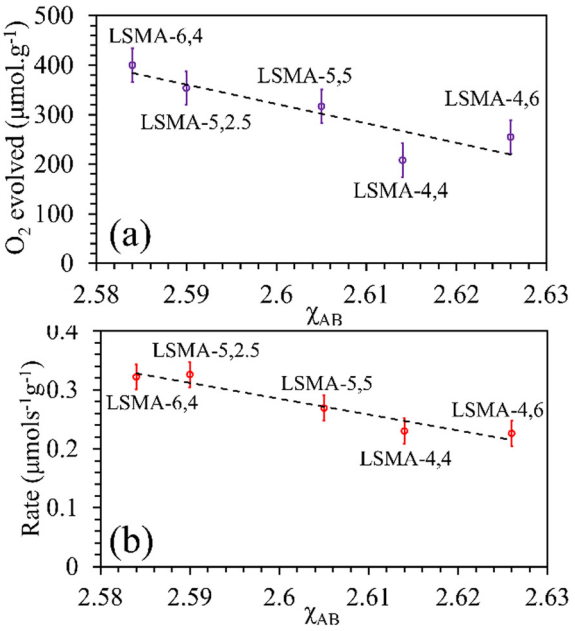

Fig. 7 Amounts of O_2 evolved (a) and reduction rates (b) as a function of overall electronegativity of cationic components for $La_xSr_{1-x}Mn_yAl_{1-y}O_3$ oxygen carriers.

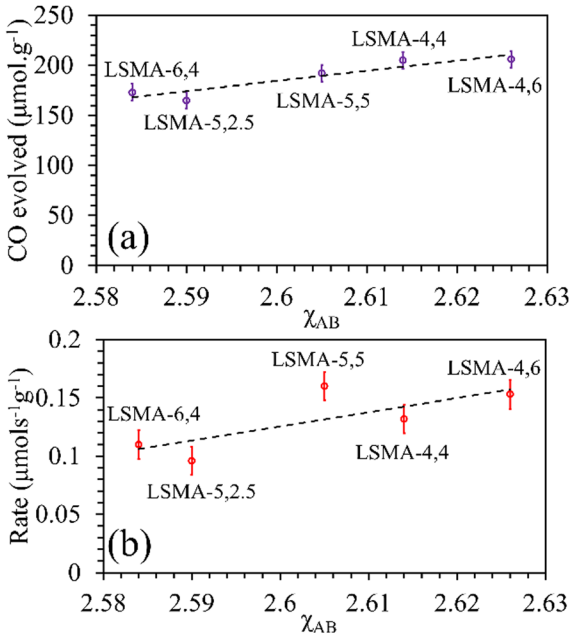

Fig. 8 Amounts of CO evolved (a) and re-oxidation rates (b) as a function of overall electronegativity of cationic components for $La_xSr_{1-x}Mn_yAl_{1-y}O_3$ oxygen carriers.

components incorporated in the $La_xSr_{1-x}Mn_yAl_{1-y}O_3$ according to eqn (7). Interestingly, in this case, a clear decrease in values of O_2 evolved and reduction rates was observed with an increase in overall cation electronegativity. Very good correlations were observed for the experimental trends with the calculated values of χ_{AB}, as shown in Fig. 7. As mentioned above, an increase in χ_{AB} indicates a decrease in metal–oxygen bond polarity, thereby hindering oxygen vacancy formation, among the series of $La_xSr_{1-x}Mn_yAl_{1-y}O_3$ oxygen carriers studied. Furthermore, the impact of cation electronegativities for CO evolution was also assessed. In this case, the amount of CO evolved was directly proportional to χ_{AB} and superior correlations were observed, as shown in Fig. 8. This is exactly reverse to the trends observed during O_2 evolution, which hence satisfactorily explains the behaviour of O_2/CO evolution shown in Fig. 2. In short, the calculated values of overall electronegativities effectively predict the thermochemical reduction and CO_2 induced re-oxidation for the series of oxygen carriers considered in this study, thus clearly indicating the existence of synergy between the cationic components in the oxygen carriers.

Metal–oxygen bond energy (λ) represents the energy required to break metal–oxygen bonds and hence can be considered as an effective parameter reflecting the oxygen transport in perovskite oxides. In other words, the calculated values of λ reflect the binding energy of oxygen with A/B-site metal cations in the perovskite lattice. Several studies previously used the calculated values of average metal–oxygen bond energies as a tool to describe the behaviour of perovskites as catalysts, electrolytes, *etc.*[32–34,39,40] In the present study, metal–oxygen bond energy (λ) was calculated using eqn (8), where C_N is the coordination number of the metal, ΔH_f is the heat of formation of M_mO_n (M = A or B), ΔH_s is the heat of sublimation of the metal and D_o is the dissociation energy of oxygen.[41,42]

$$\lambda_{M-O} = (1/C_N{\cdot}m){\cdot}[\Delta H_f - m{\cdot}\Delta H_s - (n/2){\cdot}D_o] \quad (8)$$

$$\lambda_{A-O} = x \times \lambda_{La-O} + (1 - x) \times \lambda_{Sr-O} \quad (9)$$

$$\lambda_{B-O} = y \times \lambda_{Mn-O} + (1 - y) \times \lambda_{Al-O} \quad (10)$$

First, we tried to correlate the values λ_{A-O} and λ_{B-O} separately with the amounts of O_2 released and the thermal reduction rates. The values of ionic radii of the cationic constituents compiled by Shannon[31] were used for calculating the molar average of metal–oxygen bond energies using eqn (8)–(10) and the obtained profiles are shown in Fig. S14–S17 (ESI†). Indeed, the values of bond energies corresponding to individual cationic constituents were not sufficient to describe the behaviour of O_2 evolution in these perovskites. For example, LSMA-5,2.5 and LSMA-5,5 have same values of λ_{A-O}. However, the amounts of oxygen evolved from them were different (ESI,† Fig. S14). Therefore, we calculated the overall bond energies (λ) comprising all the cations incorporated in A and B-sites of the $La_xSr_{1-x}Mn_yAl_{1-y}O_3$ structure. In this case, an inverse relationship was observed between oxygen evolution and λ. Obviously, oxygen release will be more facilitated by a weaker bond.

Satisfactory correlations were observed for the experimentally observed O_2 evolution tendencies, as shown in Fig. 9. In a similar manner, no specific influence was evident for individual bond energies (λ_{A-O} and λ_{B-O}) in CO_2 induced re-oxidation.

In contrast, both the amounts of CO evolved and the re-oxidation rates were very well correlated with the calculated values of overall bond energies (λ), exhibiting superior correlations,

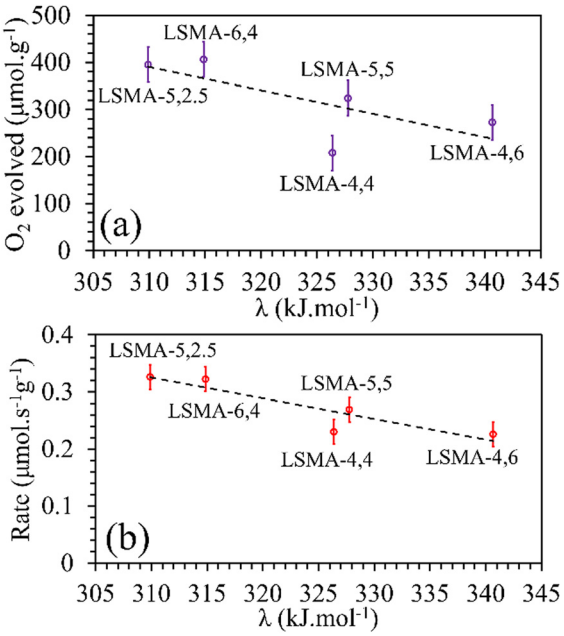

Fig. 9 Amounts of O_2 evolved (a) and reduction rates (b) as a function of overall bond energies for $La_xSr_{1-x}Mn_yAl_{1-y}O_3$ oxygen carriers.

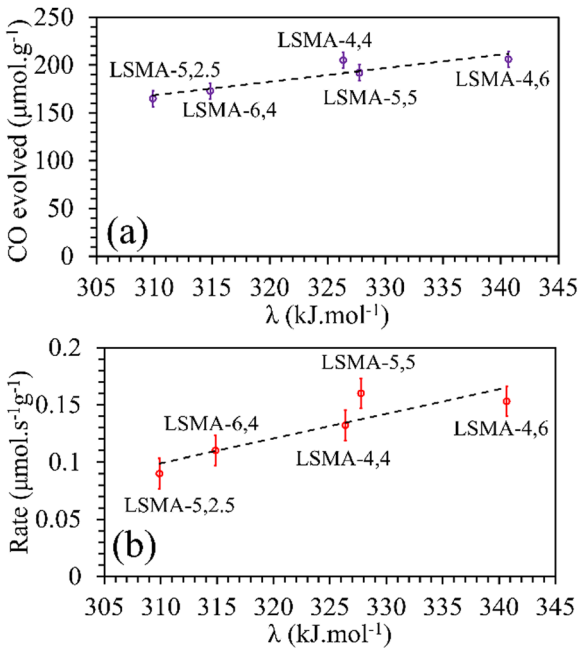

Fig. 10 Amounts of CO evolved (a) and re-oxidation rates (b) as a function of overall bond energies for a series of $La_xSr_{1-x}Mn_yAl_{1-y}O_3$ oxygen carriers.

as shown in Fig. 10. Similar to the observations in the case of electronegativity, a reversal in trends was visible for the distributions of O_2 evolution and CO evolution against λ, in agreement with the results in Fig. 2. This result further confirms the suitability of overall bond energy as an effective descriptor for thermochemical reduction and CO_2 induced re-oxidation for the oxygen carriers investigated in the present study. Additionally,

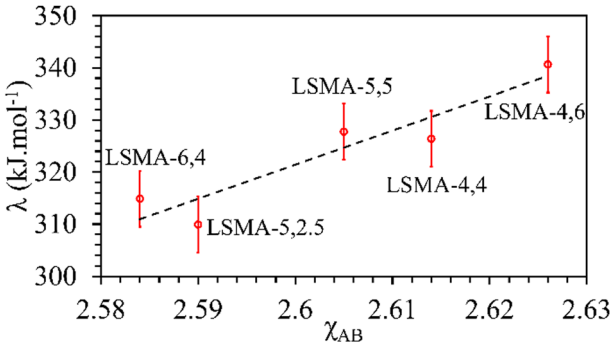

Fig. 11 Calculated values of overall metal–oxygen bond energies as a function of overall cation electronegativities for a series of $La_xSr_{1-x}Mn_yAl_{1-y}O_3$ oxygen carriers.

these results confirm the synergistic contribution of the individual cationic constituents in depicting the thermochemical redox properties. Thus, overall electronegativity (χ_{AB}) and overall metal–oxygen bond energy (λ) are found to be the most suitable parameters for describing the thermochemical redox activity of $La_xSr_{1-x}Mn_yAl_{1-y}O_3$ oxygen carriers. This was further confirmed by a plot of bond energies as a function of cation electronegativities. As shown in Fig. 11, the bond energy increased with an increase in the values of electronegativity.

Tailoring the redox functionalities of oxygen carriers plays a major role in advancing the thermochemical redox processes for concentrated solar energy applications. Fundamental understanding of the reaction mechanisms along with identification of the crucial parameters controlling the redox behaviour will be a major objective in this regard. In mixed oxide oxygen carriers, a seemingly facile approach will be the selection of appropriate cationic components in adequate concentrations. However, in perovskites, experimental determination of appropriate formulations is rather complex considering the plethora of elements that can occupy the cationic sites in varying amounts. This offers the room for identifying a suitable descriptor to carry out an initial screening while selecting the formulation. Preliminary information regarding the formation, stability and structural distortion in ABO_3 materials can be obtained from the tolerance factor (τ). A straightforward calculation of τ can be achieved by using the ionic radii of the constituents, (see eqn (2)). As mentioned before, the values of τ imply deviations from the ideal cubic crystal structure ($\tau = 1$). Larger deviations from unity result in the collapse of the ABO_3 structure, resulting in the formation of binary oxides or related structural variants. It is to be noted that the thermochemical release of lattice oxygen results in changes in the transition metal oxidation state and hence the ionic radii during the reaction. Therefore, initial selection of the cationic components of the perovskite structure should be made with minimum deviation from the value of unity for tolerance factor, so as to accommodate structural variations during the reduction and re-oxidation reactions. Among the series of oxygen carriers used in this study, conclusive trends were not observed for O_2/CO evolution as a function of tolerance factor. Therefore, apart

from preliminary information regarding material formation and stability, it can be concluded that this parameter has a negligible influence to predict the redox behaviour of perovskite oxygen carriers. In general, the thermochemical reduction and the subsequent re-oxidation can follow different mechanisms. The critical radius per unit cell volume was previously found to identify the O_2 evolution behaviour whereas, CO_2 splitting tendencies were better defined by the values of lattice free volumes, among a series of A-site substituted perovskites ($La_{1-x}A_xMnO_3$).[19] In that case, only A-site composition was varied, implying geometrical modifications as the predominant consequence, and the redox active center (Mn) remained the same. Moreover, no inverted trends were evidenced from the O_2/CO evolution profiles. In contrast, both A and B-site compositions in the perovskites were simultaneously changed in the present study and thus variations in both structural aspects and redox active sites were inevitable. This can be a reason why parameters denoting structural changes (τ, R_c, and V_F) alone did not satisfactorily reflect the observed redox performance trends.

Apart from structural parameters, bond polarity aspects were also considered to correlate the thermochemical oxygen release/uptake behaviour of perovskites. Indicating the presence of synergistic interactions between the cationic components, the molar average of electronegativities was found to correlate well with O_2/CO evolution trends. Similarly, the overall values of metal–oxygen bond energy were also found to satisfactorily correspond to the thermochemical redox reaction trends in perovskite oxides considered in this study. Previous studies indicated a composition dependence of oxygen vacancy formation energy in perovskites, making them a favourable choice as oxygen carriers for solar thermochemical fuel production.[10,23,43–45] Pearson cross-correlation analysis involving all the variables used in this study was performed separately for solar thermal O_2 evolution and CO_2 splitting, and the resultant correlation matrices are provided in Fig. 12. The values of Pearson coefficients (r) generally vary between +1 and −1, where +1 indicate a direct linear correlation and −1 indicate an inverse linear correlation. Values above 0.80 (or below −0.80) indicate strong correlation while the values closer to 0 mean poor correlation.[46–48] Strong inverse correlations were observed for the rates of oxygen evolution with overall electronegativity and metal–oxygen bond energies, with r values of −0.96 and −0.90, respectively. Similarly, strong direct linear correlations were observed for the rates of CO_2 splitting with overall electronegativity and metal–oxygen bond energies, with r values of 0.78 and 0.91, respectively. It is to be noted here that strong correlations were observed for other parameters also. However, in this case, the condition for inverted trends in O_2/CO evolution was not satisfied. Therefore, bond polarity can be considered as a simple and convenient parameter for the initial selection of oxygen carriers in solar thermochemical processes.

Varying the amount of Sr and Fe in A and B-sites, respectively, was found to modify the oxygen vacancy formation energy in perovskites. In $La_xSr_{1-x}Mn_yAl_{1-y}O_3$, substitution of

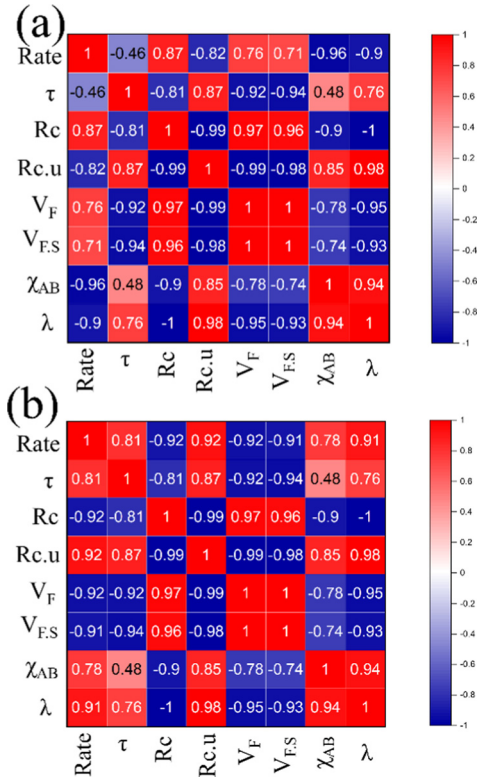

Fig. 12 Pearson correlation matrices indicating the relationship between different parameters used for (a) oxygen evolution and (b) CO_2 splitting.

Sr^{2+} in the La^{3+} site results in holes and shifts the Fermi energy with respect to the O 2p band center. Also, the changes in the Mn concentration in the B-site tunes the mixed Mn 3d–O 2p band, accommodating a larger shift in Fermi energy. The findings of the present study clearly show that the variations in O_2 and CO evolutions were suitably described by the overall cationic composition of the A and B-sites, at least for the series of materials and reaction conditions used. Moreover, this study proposes the use of bond polarity as indicated by cation electronegativity or metal–oxygen bond energy as appropriate metrics to screen multi-component perovskite oxides for applications in thermochemical redox reactions. In addition to the material design criteria based on thermodynamic parameters,[49] the use of such simple parameters can aid in the preliminary selection of oxygen carrier compositions.

4. Conclusion

Perovskite structured oxygen carriers with varying amounts of strontium and aluminium in the A and B sites, respectively, were studied regarding their thermochemical O_2 evolution and CO_2 splitting efficiencies. Since cation composition was the sole variable throughout the redox experiments, the changes in gas evolution tendencies can be attributed to the same. Cation substitution can induce structural distortions in perovskite oxides and can thereby influence the vacancy formation and ion mobility in the crystal lattice. The factors selected in this

study reflect the extent of such distortions and their influence on the oxygen uptake and release during thermochemical redox cycles. Geometric parameters such as tolerance factor (τ), critical radius (R_c) and lattice free volume (V_F) were found not to be suitable to depict the observed thermochemical redox reaction trends. In contrast, direct relationships between the calculated values of cation electronegativities (χ) and metal–oxygen bond energies (λ) with experimental O_2/CO evolution were observed. In this case, an overall contribution incorporating all the cationic constituents was found to be necessary. Lower values of overall cation electronegativities (or metal–oxygen bond energies) favoured oxygen release from $La_xSr_{1-x}Mn_yAl_{1-y}O_3$ oxygen carriers, whereas higher values favoured oxygen uptake during CO_2 induced re-oxidation. The proposed cation dependent parameters are expected to accelerate the design of perovskite oxygen carriers for thermochemical redox processes utilizing concentrated solar energy in the future.

Author contributions

Conceptualization: M. M. N. and S. A.; data curation: M. M. N. and S. A.; formal analysis: M. M. N. and S. A.; investigation: M. M. N. and S. A.; methodology: M. M. N. and S. A.; project administration: S. A.; supervision: S. A.; validation: M. M. N. and S. A.; visualization: M. M. N.; writing original draft: M. M. N.; writing review and editing: S. A.

Conflicts of interest

There are no conflicts to declare.

Acknowledgements

This study was supported by the French National Agency for Research (ANR, SUNFUEL project, contract no. ANR-16-CE06-0010-01).

Notes and references

1 J. Vieten, B. Bulfin, P. Huck, M. Horton, D. Guban, L. Zhu, Y. Lu, K. A. Persson, M. Roeb and C. Sattler, *Energy Environ. Sci.*, 2019, **12**, 1369.
2 M. Kubicek, A. H. Bork and J. L. M. Rupp, *J. Mater. Chem. A*, 2017, **5**, 11983.
3 L. Zeng, Z. Cheng, J. A. Fan, L. Fan and J. Gong, *Nat. Rev. Chem.*, 2018, **2**, 349.
4 C. L. Muhich, B. W. Evanko, K. C. Weston, P. Lichty, X. Liang, J. Martinek, C. B. Musgrave and A. W. Weimer, *Science*, 2013, **341**, 540.
5 W. C. Chueh, C. Falter, M. Abbott, D. Scipio, P. Furler, S. M. Haile and A. Steinfeld, *Science*, 2010, **330**, 1797.
6 P. Furler, J. R. Scheffe and A. Steinfeld, *Energy Environ. Sci.*, 2012, **5**, 6098.
7 M. Takacs, J. R. Scheffe and A. Steinfeld, *Phys. Chem. Chem. Phys.*, 2015, **17**, 7813.
8 A. Le Gal, S. Abanades and G. Flamant, *Energy Fuels*, 2011, **25**, 4836.
9 L. Wang, M. Al-Mamun, Y. L. Zhong, L. Jiang, P. Liu, Y. Wang, H. G. Yang and H. Zhao, *Sustainable Energy Fuels*, 2017, **1**, 1013.
10 G. Voitic and V. Hacker, *RSC Adv.*, 2016, **6**, 98267.
11 Y. Chen, X. Zhu, K. Li, Y. Wei, Y. Zheng and H. Wang, *ACS Sustainable Chem. Eng.*, 2019, **7**, 15452.
12 J. R. Scheffe, D. Weibel and A. Steinfeld, *Energy Fuels*, 2013, **27**, 4250.
13 M. M. Nair and S. Abanades, *ChemistrySelect*, 2016, **1**, 4449.
14 M. M. Nair and S. Abanades, *Sustainable Energy Fuels*, 2018, **2**, 843.
15 A. Demont and S. Abanades, *J. Mater. Chem. A*, 2015, **3**, 3536.
16 A. Riaz, P. Kreider, F. Kremer, H. Tabassum, J. S. Yeoh, W. Lipinski and A. Lowe, *ACS Appl. Energy Mater.*, 2019, **2**, 2494.
17 L. Liu, D. D. Taylor, E. E. Rodriguez and M. R. Zachariah, *Chem. Commun.*, 2016, **52**, 10369.
18 X. Wang, T. Wu and M. R. Zachariah, *J. Phys. Chem. C*, 2017, **121**, 147.
19 M. M. Nair and S. Abanades, *Sustainable Energy Fuels*, 2021, **5**, 4570.
20 J. P. Attfield, *Chem. Mater.*, 1998, **10**, 3239.
21 A. V. Shlyakhtina and K. S. Pigalskiy, *Mater. Res. Bull.*, 2019, **116**, 72.
22 A. H. McDaniel, E. C. Miller, D. Arifin, A. Ambrosini, E. N. Coker, R. O'Hayre, W. C. Chueh and J. Tong, *Energy Environ. Sci.*, 2013, **6**, 2424.
23 A. M. Deml, V. Stevanovic, A. M. Holder, M. Sanders, R. O'Hayre and C. B. Musgrave, *Chem. Mater.*, 2014, **26**, 6595.
24 M. Ezbiri, M. Takacs, D. Theiler, R. Michalsky and A. Steinfeld, *J. Mater. Chem. A*, 2017, **5**, 4172.
25 T. Cooper, J. R. Scheffe, M. E. Galvez, R. Jacot, G. Patzke and A. Steinfeld, *Energy Technol.*, 2015, **3**, 1130.
26 M. E. Galvez, R. Jacot, J. R. Scheffe, T. Cooper, G. Patzke and A. Steinfeld, *Phys. Chem. Chem. Phys.*, 2015, **17**, 6629.
27 M. Ezbiri, V. Becattini, M. Hoes, R. Michalsky and A. Steinfeld, *ChemSusChem*, 2017, **10**, 1517.
28 M. Takacs, M. Hoes, M. Caduff, T. Cooper, J. R. Scheffe and A. Steinfeld, *Acta Mater.*, 2016, **103**, 700.
29 J. P. Attfield, *Int. J. Inorg. Mater.*, 2001, **3**, 1147.
30 M. R. Filip and F. Giustino, *Proc. Natl. Acad. Sci. U. S. A.*, 2018, **115**, 5397.
31 R. D. Shannon, *Acta Crystallogr.*, 1976, **A32**, 751.
32 S. Li, W. Jin, P. Huang, N. Xu and J. Shi, *Ind. Eng. Chem. Res.*, 1999, **38**, 2963.
33 R. L. Cook and A. F. Sammells, *Solid State Ionics*, 1991, **45**, 311.
34 A. F. Sammells, R. L. Cook, J. H. White, J. J. Osborne and R. C. MacDuff, *Solid State Ionics*, 1992, **52**, 111.
35 N. Xu, H. Zhao, X. Zhou, W. Wei, X. Lu, W. Ding and F. Li, *Int. J. Hydrogen Energy*, 2010, **35**, 7295.
36 H. Hayashi, H. Inaba, M. Matsuyama, N. G. Lan, M. Dokiya and H. Tagawa, *Solid State Ionics*, 1999, **122**, 1.

37 M. Mogensen, D. Lybye, N. Bonanos, P. V. Hendriksen and F. W. Poulsen, *Solid State Ionics*, 2004, **174**, 279.
38 L. Pauling, *J. Am. Chem. Soc.*, 1932, **54**, 3570.
39 G. M. Dhar and V. Srinivasan, *Int. J. Chem. Kinet.*, 1982, **14**, 435.
40 M. Futai, Y. Chen and L. Hui, *React. Kinet. Catal. Lett.*, 1986, **31**, 47.
41 R. A. Robie, B. S. Hemingway and J. R. Fisher, *U.S. Geol. Surv. Bull.*, 1979, **1452**, 1.
42 D. D. Wagman, W. H. Evans, V. B. Parker, R. H. Schumm, I. Halow, S. M. Bailey, K. L. Churney and R. L. Nuttall, The NBS tables of chemical thermodynamic properties, *J. Phys. Chem. Ref. Data*, 1982, **11**, 1.
43 Y. A. Mastrikov, R. Merkle, E. A. Kotomin, M. M. Kuklja and J. Maier, *Phys. Chem. Chem. Phys.*, 2013, **15**, 911.
44 E. A. Kotomin, Y. A. Mastrikov, M. M. Kuklja, R. Merkle, A. Roytburd and J. Maier, *Solid State Ionics*, 2011, **188**, 1.
45 M. Pavone, A. B. Munoz-García, A. M. Ritzmann and E. A. Carter, *J. Phys. Chem. C*, 2014, **118**, 13346.
46 I. Gomez-Recio, H. Pan, A. Azor-Lafarga, M. L. Ruiz-Gonzalez, M. Hernando, M. Parras, M. T. Fernandez-Diaz, J. J. Delgado, X. Chen, D. G. Jimenez, D. Portehault, C. Sanchez, M. Cabero, A. Martinez-Arias, J. M. Gonzalez-Calbet and J. J. Calvino, *ACS Catal.*, 2021, **11**, 15026.
47 T. W. Walker, A. K. Chew, H. Li, B. Demir, Z. C. Zhang, G. W. Huber, R. C. Van Lehn and J. A. Dumesic, *Energy Environ. Sci.*, 2018, **11**, 617.
48 Y. Zhong, X. Liang, Z. He, W. Tan, J. Zhu, P. Yuan, R. Zhu and H. He, *Appl. Catal., B*, 2014, **150**, 612.
49 A. Bayon, A. de la Calle, E. B. Stechel and C. Muhich, *Energy Technol.*, 2022, **10**, 2100222.